




Eliminating polarization leakage effect for neutral hydrogen intensity mapping with deep learning

Li-Yang Gao ¹, Yichao Li ¹*, Shulei Ni ¹, Xin Zhang ^{1,2,3}†

¹ Key Laboratory of Cosmology and Astrophysics (Liaoning) & College of Sciences, Northeastern University, Shenyang 110819, China

² Key Laboratory of Data Analytics and Optimization for Smart Industry (Ministry of Education), Northeastern University, Shenyang 110819, China

³ National Frontiers Science Center for Industrial Intelligence and Systems Optimization, Northeastern University, Shenyang 110819, China

6 September 2023

ABSTRACT

The neutral hydrogen (HI) intensity mapping (IM) survey is regarded as a promising approach for cosmic large-scale structure studies. A major issue for the HI IM survey is to remove the bright foreground contamination. A key to successfully removing the bright foreground is to well control or eliminate the instrumental effects. In this work, we consider the instrumental effects of polarization leakage and use the U-Net approach, a deep learning-based foreground removal technique, to eliminate the polarization leakage effect. The thermal noise is assumed to be a subdominant factor compared with the polarization leakage for future HI IM surveys and ignored in this analysis. In this method, the principal component analysis (PCA) foreground subtraction is used as a preprocessing step for the U-Net foreground subtraction. Our results show that the additional U-Net processing could either remove the foreground residual after the conservative PCA subtraction or compensate for the signal loss caused by the aggressive PCA preprocessing. Finally, we test the robustness of the U-Net foreground subtraction technique and show that it is still reliable in the case of existing constraint error on HI fluctuation amplitude.

Key words: polarization – techniques: image processing – methods: data analysis

1 INTRODUCTION

Measurements of cosmic large-scale structure (LSS) are critical for understanding the evolutionary history of the Universe. In recent decades, the LSS fluctuation of the underlying dark matter has been explored by mapping the galaxies' distribution in the Universe using wide-field spectroscopic and photometric surveys (e.g. [Beutler et al. 2011](#); [Ross et al. 2015](#); [Alam et al. 2017](#)). The cosmic LSS can also be probed at radio bands by observing the neutral hydrogen (HI) in galaxies via its 21 cm emission line of hyperfine spin-flip transition (e.g. [Battye et al. 2004](#); [McQuinn et al. 2006](#); [Loeb & Wyithe 2008](#)). Instead of resolving the HI emission line from each distant galaxy, the LSS HI survey can be quickly carried out by measuring the total HI intensity of many galaxies within a large voxel. Such LSS survey technique is known as HI intensity mapping (IM) ([McQuinn et al. 2006](#); [Loeb & Wyithe 2008](#); [Mao et al. 2008](#); [Lidz et al. 2011](#); [Battye et al. 2013a](#)), which is ideal for cosmological studies. (e.g. [Xu et al. 2015](#); [Bull et al. 2015](#); [Yohana et al. 2019](#); [Zhang et al. 2019, 2020](#); [Xu & Zhang 2020](#); [Gao et al. 2021](#); [Wu & Zhang 2022](#); [Zhang et al. 2021](#); [Wu et al. 2022b](#); [Jin et al. 2021](#); [Wu et al. 2022a](#); [Jin et al. 2020](#)).

Since the first detection of the cross-correlation function between the HI IM survey and the optical galaxy survey using Green Bank Telescope ([Chang et al. 2010](#)), there are a number of measurements of the cross-correlation power spectrum between HI IM survey and optical galaxy survey (e.g. [Masui et al. 2013](#); [Anderson et al. 2018](#);

[Wolz et al. 2017, 2021](#); [CHIME Collaboration et al. 2022](#)). Moreover, several radio telescopes and interferometers specially designed for HI IM survey are either under construction or collecting data, i.e., the Tianlai project ([Chen 2012](#); [Li et al. 2020](#); [Wu et al. 2021](#); [Perdereau et al. 2022](#); [Sun et al. 2022](#)), the Canadian Hydrogen Intensity Mapping Experiment (CHIME, [Bandura et al. 2014](#)), the Baryonic Acoustic Oscillations from Integrated Neutral Gas Observations (BINGO, [Battye et al. 2013b](#)) and the Hydrogen Intensity and Real-Time Analysis experiment (HIRAX, [Newburgh et al. 2016](#)). The HI IM survey is also proposed as a major cosmological probe using the Square Kilometre Array (SKA, [Santos et al. 2015](#)), and its pathfinder array, MeerKAT ([Santos et al. 2017](#); [Li et al. 2021](#); [Wang et al. 2021](#)). Recently, [Cunnington et al. \(2023\)](#) reported the detection of cross-correlation power spectrum of the MeerKAT HI IM survey and the WiggleZ optical galaxy survey. Meanwhile, using the MeerKAT interferometric observations, [Paul et al. \(2023\)](#) reported the HI IM auto-correlation power spectrum detection on Mpc scales.

However, there still are challenges for HI IM cosmological studies. The auto-correlation power spectrum of the HI fluctuation on large scales has not yet been detected with the IM survey at this time ([Switzer et al. 2013](#)). The main challenge for this observation method is to extract the HI LSS signal from the bright foreground contamination, e.g. the Galactic synchrotron emission, the Galactic free-free emission, and the extragalactic radio sources ([Cunnington et al. 2021](#); [Spinelli et al. 2021](#); [Wolz et al. 2015](#)). Although this task may be impossible at first, it has been proposed that the smooth frequency dependence of the foreground can be used to separate them from the faint HI LSS signal ([Bowman et al. 2009](#); [Ansari et al. 2012](#)). For example, [Ansari et al. \(2012\)](#); [Bigot-Sazy et al. \(2015\)](#)

* E-mail: liyichao@mail.neu.edu.cn

† E-mail: zhangxin@mail.neu.edu.cn

used non-blind parametric fitting to remove the foregrounds. [Shaw et al. \(2014\)](#) implemented the Karhunen Loève (KL) transform for foreground subtraction, which extracts the HI signal by modeling the statistical properties of various components of the sky (e.g., signal, foreground, and noise). However, the instrumental effects, existing in all radio telescope systems, significantly increase the difficulty and complexity of such components separation technique ([Matshawule et al. 2021](#); [Spinelli et al. 2022](#)). To address the instrumental effects, a couple of blind foreground subtraction approaches have been developed, such as the Principal Component Analysis (PCA, [Masui et al. 2013](#)), the Fast Independent Component Analysis (FASTICA, [Chapman et al. 2012](#); [Cunnington et al. 2019](#); [Wolz et al. 2014](#); [Hyvarinen 1999](#)), and Generalised Morphological Component Analysis (GMCA, [Bobin et al. 2007](#)). Especially, the PCA and FastICA methods are already applied to the real HI IM survey data ([Masui et al. 2013](#); [Anderson et al. 2018](#); [Wolz et al. 2021](#); [Patil et al. 2017](#)). We emphasize that our list of methods is not an exhaustive list and there are probably many more methods that can be used for foreground removal of HI IM.

The instrumental effect complicates the structure of the foreground spectrum. Thus, eliminating the instrumental effect is crucial for efficiently removing the foreground. When considering the instrumental effect, the rapidly growing deep learning algorithm can play a critical role in foreground subtraction ([Goodfellow et al. 2016](#)). Deep learning has been widely used in cosmology and radio astronomy, such as using deep learning to predict the cosmological structure formation ([He et al. 2019](#)), generating HI mock signals ([Wadekar et al. 2021](#)), simulating and exploring cosmic dawn and epoch of reionization ([Gillet et al. 2019](#); [Kwon et al. 2020](#); [List & Lewis 2020](#); [Mangena et al. 2020](#); [Villanueva-Domingo & Villaescusa-Navarro 2021](#)), etc. In the meanwhile, deep learning can also be used in foreground subtraction ([Li et al. 2019](#)). [Makinen et al. \(2021\)](#) reported a foreground subtraction method based on a convolutional neural network (CNN) architecture based on a 3D U-Net model ([Kohl et al. 2018](#)). [Ni et al. \(2022\)](#), for the first time, proposed a deep learning approach to eliminate the primary beam effect in HI IM foreground subtraction.

In addition to the primary beam effect, the instrumental polarization leakage also needs to be properly controlled ([Nunhokee et al. 2017](#); [Bhatnagar & Nityananda 2001](#)). Although the polarization of the HI emission is negligible, the foreground contamination, especially the bright synchrotron emission is polarized. Due to the imperfect calibration, the polarized foreground emission can leak into the total intensity. Such leakage could induce extra power and complicate the foreground spectrum. [Liao et al. \(2016\)](#) provided a detailed polarization calibration for GBT HI IM survey and showed that the polarization calibration error on boresight is well controlled. However, the polarization leakage can still be identified via the polarized beam pattern measurements. A few more studies are focusing on simulating polarization leakage for different HI experiments ([Shaw et al. 2015](#); [de Bruyn et al. 2006](#); [Schnitzeler et al. 2009](#); [Wolleben et al. 2006](#); [Nunhokee et al. 2017](#)). Eliminating the polarization leakage from the full beam pattern is important for separating the foreground from the HI signal.

In this paper, we further extend the deep-learning foreground subtraction approach to eliminate the instrumental effect of polarization leakage. This paper is organized as follows. In Section 2, we present the relevant formulae and the simulation of the sky maps. Section 3 describes the methods used to extract the HI signal. The results are discussed accordingly in Section 4 and the conclusions are presented in Section 5.

2 SIMULATION

The deep learning network is trained using a set of simulated sky maps, which are generated using the open-source package, CRIME (<http://intensitymapping.physics.ox.ac.uk/CRIME.html>) ([Alonso et al. 2014](#)). The sky maps include three main components, i.e. the HI brightness contrast, the foreground, and the leakage from the polarized foreground. In this work, we assume that the thermal noise levels of future HI experiments are subdominant with respect to the foreground residual. The noise level may also be lower than the HI fluctuation on large scales with sufficient long integration time for future large radio telescopes or interferometer arrays ([Li & Ma 2017](#)). As shown in the literature (e.g., [Makinen et al. 2021](#)), as long as samples with this noise level are included in the training set, the U-Net can handle different noise realizations at the same noise level. To simplify the simulation analysis and highlight the effect of the polarization leakage, the thermal noise is ignored in this work. A brief overview of the simulation processing is provided below.

2.1 HI brightness contrast

The HI brightness temperature contrast at redshift z is expressed as

$$T_{\text{HI}}(z, \hat{\mathbf{n}}) = 190.55 \text{ mK} \frac{\Omega_b h(1+z)^2 x_{\text{HI}}(z)}{\sqrt{\Omega_m(1+z)^3 + \Omega_\Lambda}} (1 + \delta_{\text{HI}}(z, \hat{\mathbf{n}})) \\ = \bar{T}_{\text{HI}}(z) (1 + \delta_{\text{HI}}(z, \hat{\mathbf{n}})), \quad (1)$$

where $h \equiv H_0/(100 \text{ km s}^{-1} \text{ Mpc}^{-1})$ is the dimensionless Hubble constant, $x_{\text{HI}}(z)$ is the neutral hydrogen mass fraction in terms of the total baryons, Ω_b , Ω_m and Ω_Λ denote the present baryon, total matter and dark energy density fractions, respectively, and $\delta_{\text{HI}}(z, \hat{\mathbf{n}})$ represent the redshift-space HI density contrast.

The full sky maps of the HI brightness contrast are simulated using a set of lognormal realizations with the tomographic angular power spectrum

$$C_\ell^{\text{HI}}(z_1, z_2) = \frac{2}{\pi} \int dk k^2 P_{\text{DM}}(k) W_{\ell, z_1}(k) W_{\ell, z_2}(k), \quad (2)$$

where $P_{\text{DM}}(k)$ is the present underlying dark matter power spectrum and $W_{\ell, z_i}(k)$ denotes the window function of a z -shell with the mean redshift at z_i ,

$$W_{\ell, z_i}(k) = \int dz \bar{T}_{\text{HI}}(z) \phi(z_i, z) D(z) (b(z) j_\ell(k\chi) - f(z) j_\ell''(k\chi)), \quad (3)$$

where j_ℓ is the ℓ -th spherical Bessel function, $D(z)$ is the growth factor, $f(z)$ is the growth rate, $b(z)$ is the linear bias of the HI density contrast with respect to the dark matter density field, and $\phi(z_i, z)$ is the redshift selection function centering at z_i . In this work, the simulated maps are generated across the uniform frequency slices according to $z = \nu_0/\nu - 1$, where $\nu_0 = 1420.406 \text{ MHz}$ is the HI emission rest frame frequency. The cosmological parameters are fixed to the best-fit values from [Aghanim et al. \(2020\)](#).

2.2 Unpolarized foreground components

We first consider the total intensity contamination from the foreground emission. The total foreground intensity maps are simulated using two different methods according to their different angular distribution properties, i.e. anisotropic and isotropic distribution.

Table 1. Parameters used in foreground $C_\ell(\nu_1, \nu_2)$ model adapted from Santos et al. (2005) and Alonso et al. (2014) for the pivot values $\ell_{\text{ref}} = 1000$ and $\nu_{\text{ref}} = 130$ MHz.

Foreground	A (mK ²)	β	α	ξ
Galactic synchrotron	700	2.4	2.80	4.0
Point sources	57	1.1	2.07	1.0
Galactic free-free	0.088	3.0	2.15	35
Extragalactic free-free	0.014	1.0	2.10	35

The Galactic synchrotron emission has a highly anisotropic angular structure. In the simulations, the anisotropic Galactic synchrotron emission is simulated by interpolating the Haslam map’s brightness temperature at 408 MHz (Haslam et al. 1982) to the required frequencies via

$$T_{\text{syn}}(\nu, \hat{\mathbf{n}}) = T_{\text{Haslam}}(\hat{\mathbf{n}}) \left(\frac{408 \text{ MHz}}{\nu} \right)^{\gamma(\hat{\mathbf{n}})} \quad (4)$$

where $\gamma(\hat{\mathbf{n}})$ is the direction-dependent spectra index. The $\gamma(\hat{\mathbf{n}})$ values are read from the Planck Sky Model (PSM Delabrouille et al. 2013).

In addition to the Galactic synchrotron emission, a set of isotropic foreground emissions are generated following the method proposed by Santos, Cooray, and Knox (SCK) (Santos et al. 2005). In this case, the foreground maps are simulated with the Gaussian random realization based on the angular power spectrum

$$C_\ell(\nu_1, \nu_2) = A \left(\frac{\ell_{\text{ref}}}{\ell} \right)^\beta \left(\frac{\nu_{\text{ref}}^2}{\nu_1 \nu_2} \right)^\alpha \exp \left(-\frac{\log^2(\nu_1/\nu_2)}{2\xi^2} \right), \quad (5)$$

where ξ is the frequency-space correlation length of the emission. The extragalactic point sources include both the nearby and the high-redshift radio galaxies. The angular distributions of both are assumed to be isotropic. The Galactic free-free emission is related to the electron distribution and not homogeneous. However, the free-free emission is a subdominant component across the simulation frequency range. The Galactic free-free, together with the extragalactic free-free emission, can be approximated as the isotropic foreground. Besides, the Galactic synchrotron emission at small scales below the angular resolution of the Haslam map is also simulated as an isotropic component. The parameters used in the SCK method for each of the isotropic components are listed in Table 1.

2.3 Leakage from polarized foreground

For a perfectly calibrated telescope, the measured intensity is only sensitive to the total intensity, rather than the different polarization modes Q or U. However, for more general cases of a non-ideal telescope, there is always leakage between different polarization modes. Such polarization leakage can be described via a 4×4 polarization calibration error matrix (van Straten 2004; Liao et al. 2016; Nunhokee et al. 2017). The polarization calibration error matrix needs to be measured via polarization calibration observation. To simplify the analysis, we only consider the intensity leakage from the polarized foreground components, i.e. the Stokes Q and U maps of the foreground (the Stokes V map is ignored as the circular polarization is assumed to be negligible). We also assume a constant polarization leakage fraction across the frequency band. Thus the polarization leakage is expressed as

$$T_{\text{leak}} = \epsilon_Q T_{\text{FG}}^Q + \epsilon_U T_{\text{FG}}^U, \quad (6)$$

where T_{FG}^Q and T_{FG}^U denote the Stocks Q and U maps of the polarized foreground, respectively, while ϵ_Q and ϵ_U represent the constant intensity leakage fractions from T_{FG}^Q and T_{FG}^U . Because synchrotron radiation is substantially stronger than other foreground components, we ignored the polarized components from other foreground emissions in our simulations.

The Galactic synchrotron emission is known to be partially linearly polarized (Pacholczyk 1970; Rybicki & Lightman 1986) and its polarization angle rotated due to the frequency-dependent Faraday rotation effect (Brentjens & de Bruyn 2005; Jelić et al. 2010; Moore et al. 2013). Such effect, combined with the polarization leakage of the non-ideal telescope, significantly complicates the foreground frequency structure and makes foreground subtraction difficult (Cunnington et al. 2021). We use CRIME package to generate the Galactic synchrotron Stocks Q and U maps at each frequency, which is constructed in the Faraday rotation measure space. The details for determining the polarized synchrotron emission using Faraday depth measurements are given in Alonso et al. (2014) and Oppermann et al. (2015). In Fig. 1, the simulated synchrotron stocks I, Q, and U maps are shown in the left, middle, and right panels, respectively.

Using the simulated Q and U maps, we vary the telescope polarization leakage fraction. We know from de Villiers & Cotton (2022) that the leakage from the I map to both the Q map and the U map is roughly less than 2%. The Mueller matrix is composed of multiple Ermeijer matrices multiplied by each other (Liao et al. 2016; Britton 2000), so we further consider the simple case that the Mueller matrix is a symmetric matrix. On this premise, we give the intensity leakage fractions. Firstly, we assume no polarization leakage and set both $\epsilon_U = 0$ and $\epsilon_Q = 0$. Then we keep $\epsilon_U = 0$ and set $\epsilon_Q = \{0.5\%, 1.0\%, 2.0\%\}$. Finally, we set $\epsilon_U = 1.0\%$ and $\epsilon_Q = \{0.0\%, 0.5\%, 1.0\%, 2.0\%\}$.

2.4 Combination of the sky maps

The simulated sky map is the combination of different components, i.e. the HI signal, the foreground components, and the leakage of the polarized synchrotron emission,

$$T_{\text{sky}}(\nu, \hat{\mathbf{n}}) = T_{\text{HI}} + T_{\text{unpol}} + T_{\text{leak}}. \quad (7)$$

In this work, we focus on the HI survey of the late-time Universe. Thus, the sky maps are simulated in the frequency range of 970 MHz to 1023 MHz, corresponding to the MeerKAT L-band HI IM survey (Santos et al. 2017). Each map contains 64 frequency channels. The maps are also simulated using different polarization leakage settings. The different polarization leakage settings are list as below,

- $(\epsilon_Q, \epsilon_U) = (0.0\%, 0.0\%)$;
- $(\epsilon_Q, \epsilon_U) = (0.5\%, 0.0\%)$;
- $(\epsilon_Q, \epsilon_U) = (1.0\%, 0.0\%)$;
- $(\epsilon_Q, \epsilon_U) = (2.0\%, 0.0\%)$;
- $(\epsilon_Q, \epsilon_U) = (0.0\%, 1.0\%)$;
- $(\epsilon_Q, \epsilon_U) = (0.5\%, 1.0\%)$;
- $(\epsilon_Q, \epsilon_U) = (1.0\%, 1.0\%)$;
- $(\epsilon_Q, \epsilon_U) = (2.0\%, 1.0\%)$.

3 METHOD

3.1 Traditional blind foreground subtraction method

There are different traditional foreground subtraction methods, e.g. PCA, fastICA, and GNILC, that have been tested with various HI IM surveys (Masui et al. 2013; Anderson et al. 2018; Wolz et al. 2017, 2021; CHIME Collaboration et al. 2022; Cunnington et al. 2023;

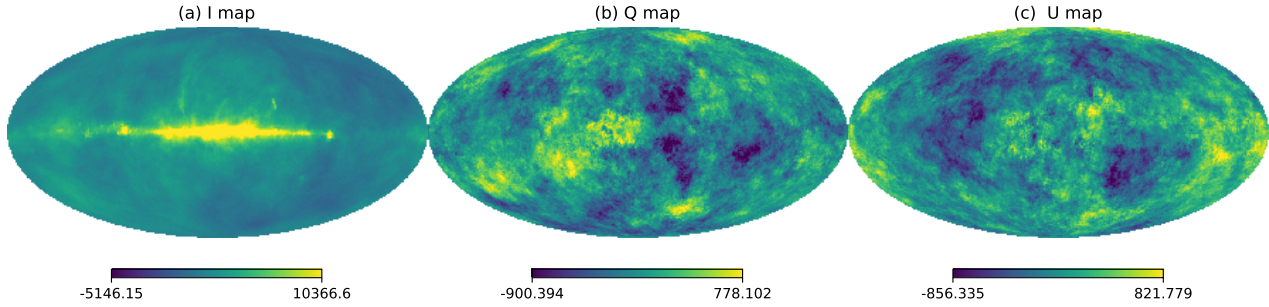


Figure 1. The sky maps of simulated Galactic synchrotron emission at the frequency of 980 MHz. The stocks I, Q, and U components are shown in the (a), (b), and (c) panels, respectively. All the maps are shown in units of mK. All of the maps in this work are drawn in Galactic coordinates using the Mollweide projection.

Olivari et al. 2016). Such blind foreground subtraction approaches can eliminate complex foreground components without requiring a thorough understanding of the systematic effect. Simulations also show that the blind foreground subtraction approaches produce similar results (Cunnington et al. 2021). In this work, we investigate the performance of the PCA approach in the presence of various polarization leakages.

The PCA approach is accomplished by doing the singular value decomposition (SVD) of the frequency-frequency covariance matrix of each line-of-sight spectra. Because the foreground components are highly correlated across frequencies as compared to the HI fluctuation, the foreground contamination is represented by the first few SVD modes with bigger singular values. The number of SVD modes to be removed depends on the complexity of the foreground spectra. A couple of effects, e.g. the antenna primary beam sidelobe (Mashawule et al. 2021), satellite communication (Harper & Dickinson 2018), polarization leakage (Cunnington et al. 2021), can significantly complicate the foreground spectra. As a result, removing a greater number of modes is required to clear up the contamination. However, such aggressive foreground subtraction always results in significant signal loss (Switzer et al. 2015).

Instead of applying aggressive foreground subtraction, we propose a light PCA foreground subtraction with additional subtraction based on the deep learning method. By subtracting only a few modes, the primary foreground contamination can be removed leaving the residual dominated by the systematic effect. Ni et al. (2022) explored such foreground subtraction approaches with a deep learning architecture to eliminate the primary beam effect in foreground subtraction. The PCA subtraction, on the other hand, is known as a crucial preprocessing step for the deep learning approach (Makinen et al. 2021).

3.2 The U-Net architecture

The 5-layers processing of the U-Net architecture is illustrated in Fig. 2. The square on the left side of the image is the cube of our input PCA-processed sky maps, while the square on the right side of the image is the data from our deep learning output. The U-Net architecture consists of down-sampling processing, shown in the left-hand-side of Fig. 2, and up-sampling processing, in the right-hand-side of Fig. 2, respectively. The down-sampling processing is a common convolutional network composed of repeated convolutional applications, each followed by a rectified linear unit (ReLU) and a maximum set operation. The convolutional layer and ReLU are illustrated with yellow boxes and the maximum set operation is shown with red boxes. With such down-sampling processing, the structure

information of the input image are contracted into a few features. An important improvement over the common convolution network is the supplementation of the up-sampling processing. The blue part represents the transposed convolution in the up-sampling process, while the grey sphere is the connection layer. The up-sampling processing combines features and spatial information through a sequence of transposed convolutions, as well as the concatenation with the down-sampled high-resolution outputs. With such up-sampling processing, the network can learn to assemble a precise HI fluctuation across the sky. It is worth noting that for the whole learning process, we use the AdamW (Loshchilov & Hutter 2017) optimizer to obtain a reasonable stepwise decreasing learning rate.

In this work, we use the U-Net architecture developed by Ronneberger et al. (2015). Currently, the U-Net package can only deal with the image data in a cube. Our full sky simulation maps need to be split into a couple of small patches.

3.2.1 Dataset assembly

The simulated full sky maps are pixelized using the HEALPIX pixelization scheme with $N_{\text{side}} = 256$. As discussed in Section 3.1, a few of the SVD modes are removed at the beginning to reduce the dynamic range of the simulated maps. We follow the same partition strategy as used in Ni et al. (2022). The SVD-modes-removed maps are split into 192 small patches across the full frequency channels, each with 64×64 pixels and 64 frequencies. The $64 \times 64 \times 64$ cubes are used as the input cubes for the U-Net network.

For each polarization leakage setting, we generate 5 different mock maps. 3 of the 5 mock maps, a total of 576 cubes, are used as the training sets, and the rest 2 mock maps are used as the verification and testing sets, respectively.

Finally, the foreground cleaned sky patches are reconstructed into the full sky maps using the same HEALPIX pixelization scheme as the input maps. We still follow the construction method implemented in Ni et al. (2022).

3.2.2 Loss function

The selection of the loss function is crucial for efficient network training. Since the standard Mean Square Error (MSE) loss function is known to be unstable in dealing with image problems (Makinen et al. 2021), and the Log-Cosh loss function is smoother than MSE. Besides, the Log-Cosh loss function is not easily influenced by anomalous points. Therefore, we use the Log-Cosh loss function

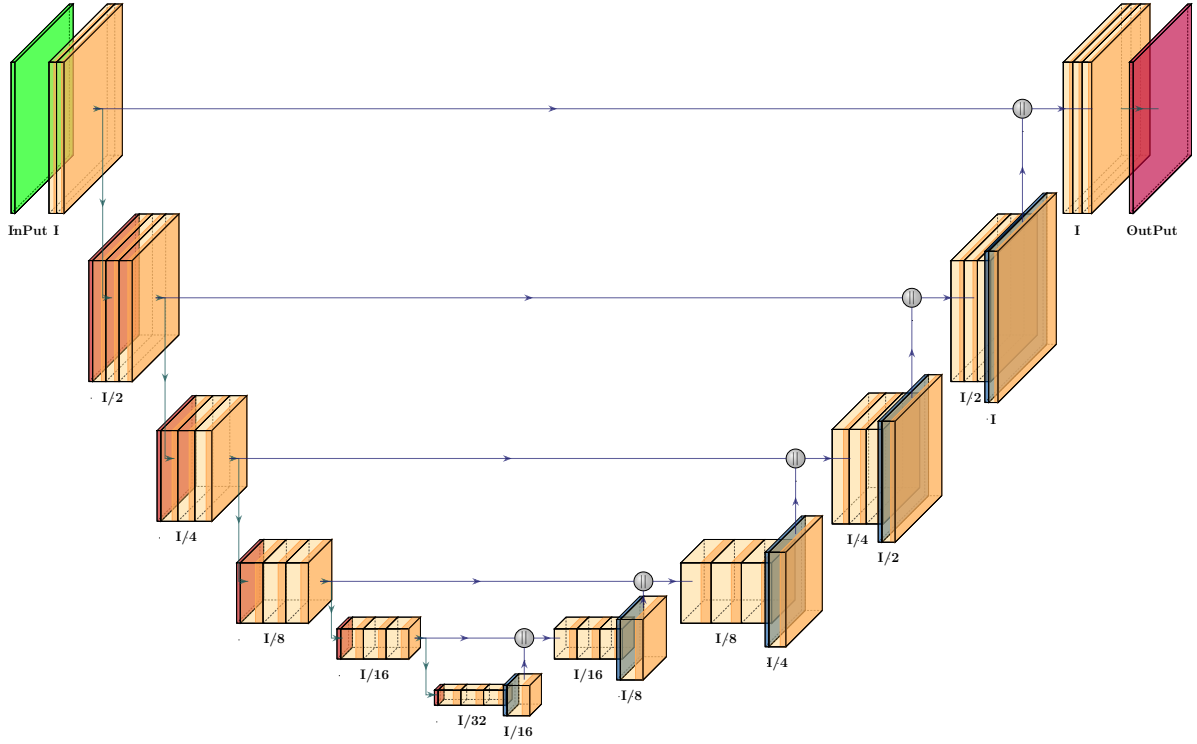


Figure 2. The training process of CNN with U-Net architecture. Each color represents a structure in the U-Net network, where yellow cubes represent the convolutional layers and ReLU sections, red cubes represent pooling layers in down-sampling, blue cubes represent the transposed convolutional layers, and grey spheres represent connection layers. The green and purple squares at the beginning and end of this figure represent the input and output, respectively.

Table 2. Description of the hyperparameters in the U-Net architecture design.

Hyperparameter	Optimum value
n_{block} (number of convolutions for each block)	3
n_{down} (number of down-convolutions)	5
n_{tc} (number of transpose convolutions)	4
batchnorm (batch normalization for given layer)	Ture*
ω (weight decay for optimizer)	10^{-5}
batch size (number of samples per gradient descent step)	16
n_{filter} (initial number of convolution filters)	36
Ω (optimizer for training)	AdamW
η (learning rate for optimizer)	10^{-3}
β_{mom} (batch normalization momentum)	0.02

in this work:

$$\mathcal{L} = \sum_i \log \cosh(p_i - t_i), \quad (8)$$

where p_i and t_i represent the predicted outcome and the true signal of the i -th voxel, respectively.

3.2.3 Hyperparameter selection

To optimize the network, the hyperparameters are fine-tuned. In order to speed up the computation of the neural network, we increase the learning rate η to 10^{-3} and increase weight decay for optimizer ω to 10^{-5} . In Fig. 3, we tested the effect of different epoch numbers. We find that the loss function does not change significantly after the epoch number reaches 20. So in this work, we used epoch = 20 for efficiency. According to the default setting, the kernel size is set to 3. We perform batch normalization for the given layer and batch

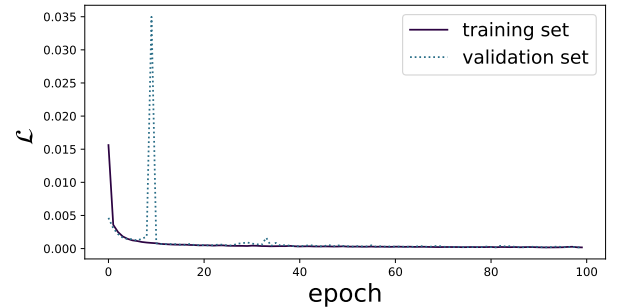


Figure 3. LogCosh loss evolves with the number of epochs. The solid line represents the evolution of the loss in the training set and the dashed line represents the evolution of the loss in the validation set.

normalization momentum ($\beta_{\text{mom}} = 1$). Besides, we use stride = 1 in the convolutions and stride = 2 in the transpose convolution, respectively. Due to the limitation of computer arithmetic, we set the batch size to 16. Since we want the neural network to be able to learn more structural information about the foreground, there is no doubt that we can improve the number of down-convolutions (n_{down}) and the initial number of convolution filters (n_{filter}). Due to the limitation of GPU memory and the little influence of n_{down} and n_{filters} on the results, we set them as 5 and 36, respectively. Therefore, because of the limitations of the neural network structure, the number of transpose convolutions (n_{tc}) equals 4. Relevant hyperparameters are represented in Table 2.

4 RESULTS AND DISCUSSION

4.1 Results with only the PCA approach

We first test the foreground subtraction with only the PCA approach. The foreground cleaned sky maps at 980 MHz with only considering the polarization leakage from the Q map are shown in Fig. 4 and with additional leakage from the U map are shown in Fig. 5. In Fig. 4 and Fig. 5, the results with different polarization leakage levels are shown in different rows. In each row, the maps with 3, 7, and 10 SVD modes subtracted are shown in the left, middle, and right panels. All the maps are shown in Galactic coordinates and in units of mK. The amplitude dynamic range of the map is truncated between $\pm 3\sigma_{\text{map}}$, where σ_{map} is the rms of the whole map.

The top row of Fig. 4 shows the cleaned sky map without any polarization leakage. Clearly, without polarization leakage, there is no obvious foreground residual structure after subtracting 3 SVD modes. We also find that even without any polarization leakage, the foreground subtraction requires at least 3 SVD modes. This is consistent with the foreground simulation analysis in the literature (e.g., Spinelli et al. 2022). When considering the polarization leakage, we assume that any foreground residuals existing in the SVD modes beyond the first 3 are due to the leakage. Such foreground residuals are further eliminated with an aggressive SVD mode subtraction in most of the HI IM experiments data analysis. In this work, we subtract the first 3 SVD modes in the pre-processing, and adopt the U-Net to eliminate the polarization leakage-induced foreground residuals.

The maps in the second, third, and fourth rows of Fig. 4 represent the results with 0.5%, 1.0%, and 2.0% polarization leakage from the Q map. The maps in Fig. 5 show the results with the same Q map polarization leakage level as the same row in Fig. 4, but with additional 1.0% polarization leakage from U map. With the polarization leakage injection, the maps with only 3 SVD modes subtracted show significant foreground residual structure. Such residual is more serious around the Galactic plane, where is highly contaminated by the foreground emission. In order to remove the residual, it needs an aggressive foreground subtraction strategy that subtracts a large number of SVD modes. As shown in the second and third columns of Fig. 4 and Fig. 5, the foreground residual is further eliminated by subtracting 7 or 10 SVD modes.

The impact of the foreground subtraction can be examined using the power spectrum. We estimate the angular power spectrum of each frequency slice and average them across the frequency band. By averaging across the frequency band, the redshift evolution of the HI LSS is marginalized. Nevertheless, the marginalization does not affect the examination of the foreground residual. The frequency-averaged angular power spectrum of the foreground cleaned maps at different polarization leakage levels are shown in different panels of Fig. 6. The corresponding leakage parameters are shown in the legend of each panel. In each panel, the black curve represents the baseline HI power spectrum estimated using the input HI map. The blue, yellow, green, and red curves represent the recovered power spectrum with 3, 4, 5, and 10 SVD modes subtracted, respectively.

As shown in the first-top panel of Fig. 6, without any polarization leakage, i.e. $(\epsilon_Q, \epsilon_U) = (0.0\%, 0.0\%)$, the foreground can be efficiently removed by subtracting a few SVD modes. Meanwhile, the recovered power spectra are well below the baseline HI power spectrum, even with only 3 SVD modes subtracted. It indicates a significant signal loss, which is a common issue for any aggressive blind foreground subtraction. The signal loss becomes more serious with even more SVD modes subtracted. The same result is even more evident in the two-dimensional power spectrum. In Fig. 7, we show the 2D power spectrum ratio of the PCA-cleaned map with

respect to the input HI map without any polarization leakage, i.e. $(\epsilon_Q, \epsilon_U) = (0.0\%, 0.0\%)$. The results of PCA-3 and PCA-4 are shown in the left and right panels, respectively. It is clear that the PCA process incorrectly subtracts part of the HI power spectrum at the lower k_{\parallel} -end, including both the lower and higher k_{\perp} , which results in an overall signal loss in the C_{ℓ} measurements.

When considering the polarization leakage, the foreground can not be efficiently removed with 3 SVD modes. As shown in the rest panels of Fig. 6, the residual is more serious at large scales, i.e. $\ell \lesssim 30$. Similar to the results shown in the map domain, the extra foreground residual can be further removed by subtracting a few more SVD modes. Fig. 6 shows that with 10 SVD mode subtraction, the foreground residual can be significantly suppressed. With the real HI IM survey data, the number of subtracted modes may be much larger than 10. For example, Masui et al. (2013) reports the cross-correlation power spectrum detection using 20 modes subtracted GBT HI IM survey maps and Cunnington et al. (2023) reports the detection of cross-correlation power spectrum using 30 modes subtracted MeerKAT HI IM survey maps. The number of SVD modes needs to be subtracted depending on the complexity of the instrumental effect. Our simulation indicates that considering the instrumental effect of polarization leakage, an aggressive PCA-based foreground subtraction method can remove the foreground.

However, it is known that the aggressive foreground subtraction results in serious signal loss (Switzer et al. 2015). As shown in Fig. 6, the power spectrum with aggressive foreground subtraction are significantly lower than the baseline HI power spectrum. The signal loss can be compensated by applying a transfer function, which is reconstructed using simulation (Switzer et al. 2015; Cunnington et al. 2023). Such transfer-function-compensation method becomes the standard analysis pipeline applied in most of the HI IM survey data analysis.

4.2 Results of PCA + U-Net

Instead of applying aggressive foreground mode subtraction, (Ni et al. 2022) proposes using the deep learning method to eliminate the foreground residual caused by the instrumental effect. According to our simulation results presented in the last section, without polarization leakage, the foreground contamination can be efficiently cleaned using the first 3 SVD modes. We assume the smooth components of the foreground can be always removed with the first 3 SVD modes and the foreground residual due to the instrumental effect contributes to the rest SVD modes. Before feeding the sky map to the U-Net, the PCA foreground subtraction is used as the pre-processing to remove the smooth components, i.e. the first 3 SVD modes. The result is shown in Fig. 8.

As an example, the reconstructed maps shown in Fig. 8 use the polarization leakage parameter ϵ_Q and ϵ_U equal to 0.5% and 1.0%, respectively. The input HI sky map is shown in the top panel. The middle panel shows the sky maps cleaned with the first 3 SVD modes, which have significant foreground residual around the Galactic plane. The bottom panel shows the reconstructed sky map with the combination of PCA-3 and U-Net. After applying the U-Net processing, the extra foreground residual structure around the Galactic plane is efficiently eliminated. The amplitude range of the map is truncated between $\pm 3\sigma_{\text{map}}$, where σ_{map} is the rms of the map. It also shows that the reconstructed map with U-Net has similar rms compared to the input HI map.

In order to highlight the foreground residuals after the processing of PCA-3 + U-Net, Fig. 9 shows the differential map between the PCA-3 + U-Net cleaned map and the input HI map, i.e. the differential

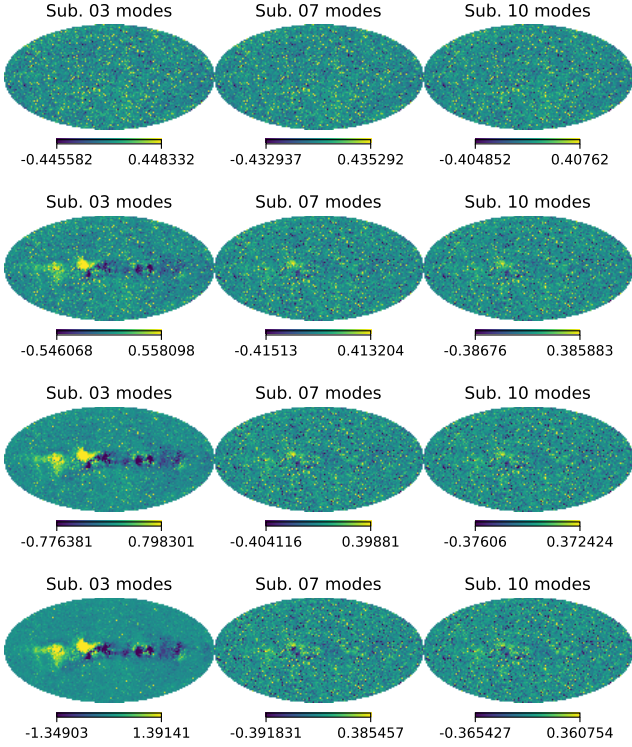


Figure 4. The PCA-only cleaned sky maps. From top to bottom, the maps with polarization leakage fraction of $(\epsilon_Q, \epsilon_U) = (0.0\%, 0.0\%), (0.5\%, 0.0\%), (1.0\%, 0.0\%)$ and $(2.0\%, 0.0\%)$ are shown in different rows. The maps with 3, 7 and 10 SVD modes subtracted are shown in the left, middle and right panels, respectively. All the maps are in units of mK.

map between Fig. 8 (c) and (a). The amplitude range of the map is also truncated between $\pm 3\sigma_{\text{map}}$. Generally, the foreground residual is low and most obvious around the Galactic plane.

The corresponding angular power spectra estimated using the reconstructed maps are shown in Fig. 10. As an example, we show the results with polarization leakage parameter ϵ_Q and ϵ_U equal to 0.5% and 1.0%, respectively, which is the same as the maps shown in Fig. 8 and Fig. 9. The angular power spectrum of the input HI map is shown with the blue curve. The yellow curve shows the angular power spectrum estimated using the map cleaned with only the first 3 SVD modes. The power spectrum estimated using the recovered HI map with the combination of PCA and U-Net is shown in green. It is clear that the extra power at large scales, which is induced from the polarization leakage, is efficiently removed with the U-Net processing. The recovered HI angular power spectrum is consistent with the input HI power spectrum.

To further confirm the authenticity of the reconstructed HI fluctuation, we estimate the cross-correlation power spectrum using the foreground cleaned map and the input HI map. In Fig. 10, the cross-correlation power spectrum result using the PCA-only cleaned map is shown with the red curve, and the result with additional U-Net processing is shown with the purple curve. Clearly, the large foreground residual of the PCA-only cleaned map significantly increases the variance of the power spectrum and results in negative values at the large-scale end. The large variance and negative power spectrum values also indicate the degrading of the correlation efficiency. However, with the additional U-Net processing, the cross-correlation angular power spectrum shows great agreement with the input HI power spectrum. The good agreement between the cross- and auto-

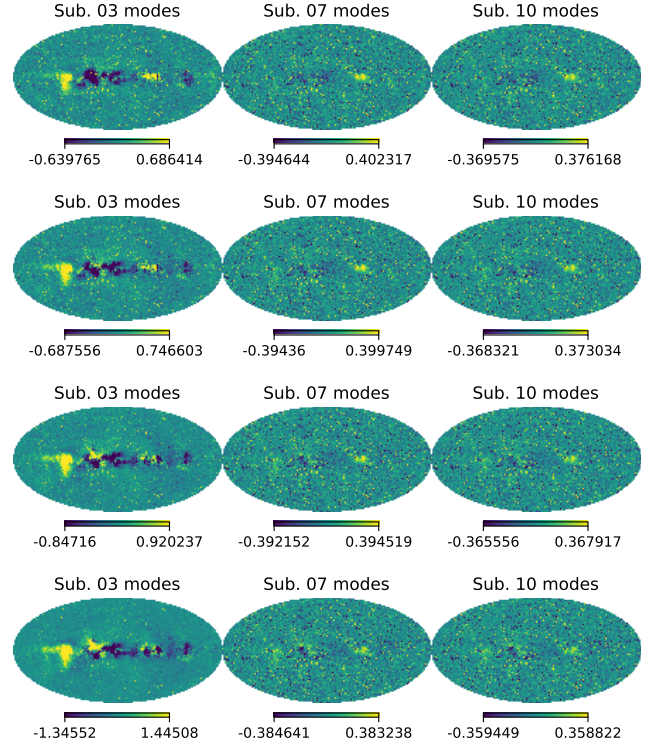


Figure 5. Same as Fig. 4 but with polarization leakage fraction of $(\epsilon_Q, \epsilon_U) = (0.0\%, 1.0\%), (0.5\%, 1.0\%), (1.0\%, 1.0\%)$ and $(2.0\%, 1.0\%)$ are shown in different rows. All the maps are in units of mK.

correlation power spectra indicate that the recovered HI map is not a fake random Gaussian field having the same power spectrum, but the truly recovered input HI map.

In order to quantify the differences between the power spectra, we employ the correlation statistic and cleaning error as defined in Makinen et al. (2021). The correlation statistic is expressed as

$$r(\ell) = \frac{P_{\text{cross}}(\ell)}{\sqrt{P_{\text{input}}(\ell)P_{\text{rec}}(\ell)}}, \quad (9)$$

and the cleaning error is

$$T(\ell) = \sqrt{\frac{P_{\text{rec}}(\ell)}{P_{\text{input}}(\ell)}}, \quad (10)$$

where $P_{\text{input}}(\ell)$ is the power spectrum of the input HI map, $P_{\text{rec}}(\ell)$ is the power spectrum of the recovered HI map and $P_{\text{cross}}(\ell)$ is the cross-correlation power spectrum between the input and recovered HI maps. The perfect recovery of the HI map results in $r(\ell) \sim 1$ and $T(\ell) \sim 1$.

Using the auto- and cross-correlation power spectra shown in Fig. 10, we estimate $r(\ell)$ and $T(\ell)$. The results are shown in Fig. 11. In each panel of Fig. 11, the result of the map recovered by subtracting only the first 3 SVD modes is shown in yellow curve and recovered with additional U-Net is shown in the blue curve. Obviously, with only 3 SVD modes subtraction, the correlation statistic deviates from 1 at the large-scale end. The deviation is mainly due to the biased auto-power spectrum and the large variance of the cross-correlation power spectrum at the large-scale end. Similarly, the cleaning error

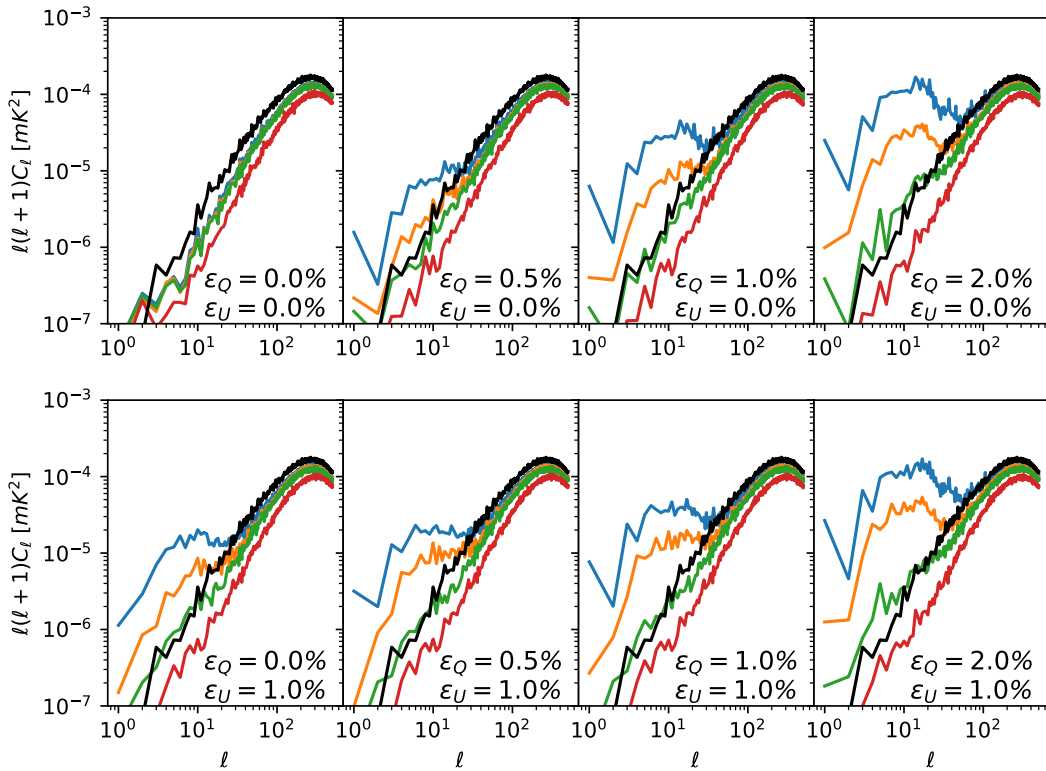


Figure 6. Angular power spectra of PCA-only cleaned sky maps. The results with different polarization leakage parameters are shown in different panels. Columns 1 to 4 represent ϵ_Q taken as 0.0%, 0.5%, 1.0%, and 2.0%, respectively. The upper and lower panels represent ϵ_U taken as 0.0% and 1.0%, respectively. The black lines represent the sky maps of the input HI signal. The blue, yellow, green, and red lines represent the power spectrum after subtracting the first 3, 4, 5, and 10 SVD modes, respectively.

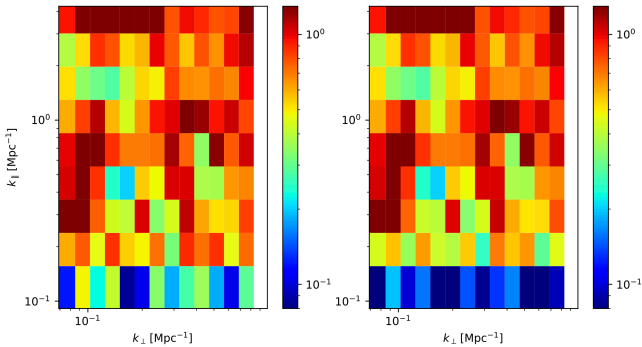


Figure 7. The ratio of the 2D power spectrum with respect to the input HI signal. Assuming no polarization leakage, i.e. $(\epsilon_Q, \epsilon_U) = (0.0\%, 0.0\%)$, the results of PCA-only foreground cleaned maps with 3 and 4 modes subtraction are shown in the left and right panels, respectively.

also shows a large deviation from 1 at the large-scale end. With the additional U-Net processing, both $r(\ell)$ and $T(\ell)$ are close to 1.

The cleaning error $T(\ell)$ for different polarization leakage parameter settings are shown in Fig. 12, where Fig. 12 (a) shows the results with different polarization leakage fraction from the Q map only and Fig. 12 (b) shows the results with additional leakage from the U map.

In both Fig. 12 (a) and (b), the results with only SVD modes subtracted are shown in the top panels and the results with extra U-Net processing are in the bottom panels. The blue, yellow, and green curves show the result with 3, 4, and 5 SVD modes subtracted, respectively. With only the first 3 SVD modes subtracted, the cleaning error shows a significant deviation from 1 at large scales with any polarization leakage fraction. Such deviation of cleaning error can be eliminated by subtracting more SVD modes but results in signal loss. On the other hand, the additional U-Net processing can efficiently eliminate the foreground residual induced by polarization leakage. The results indicate that the additional U-Net processing can recover the input HI map with different levels of polarization leakage, as well as different levels of PCA preprocessing.

4.3 Signal loss compensation

In Fig. 12 we also show the results with different numbers of SVD mode subtraction. The aggressive SVD mode subtraction can also remove the foreground leakage, but results in either signal loss or large variances in the power spectrum. However, as shown in the bottom panel of Fig. 12 (a) and (b), the cleaning error is consistent with 1 after the additional U-Net processing. It means that the additional U-Net processing can also compensate the signal killed by the aggressive PCA preprocessing.

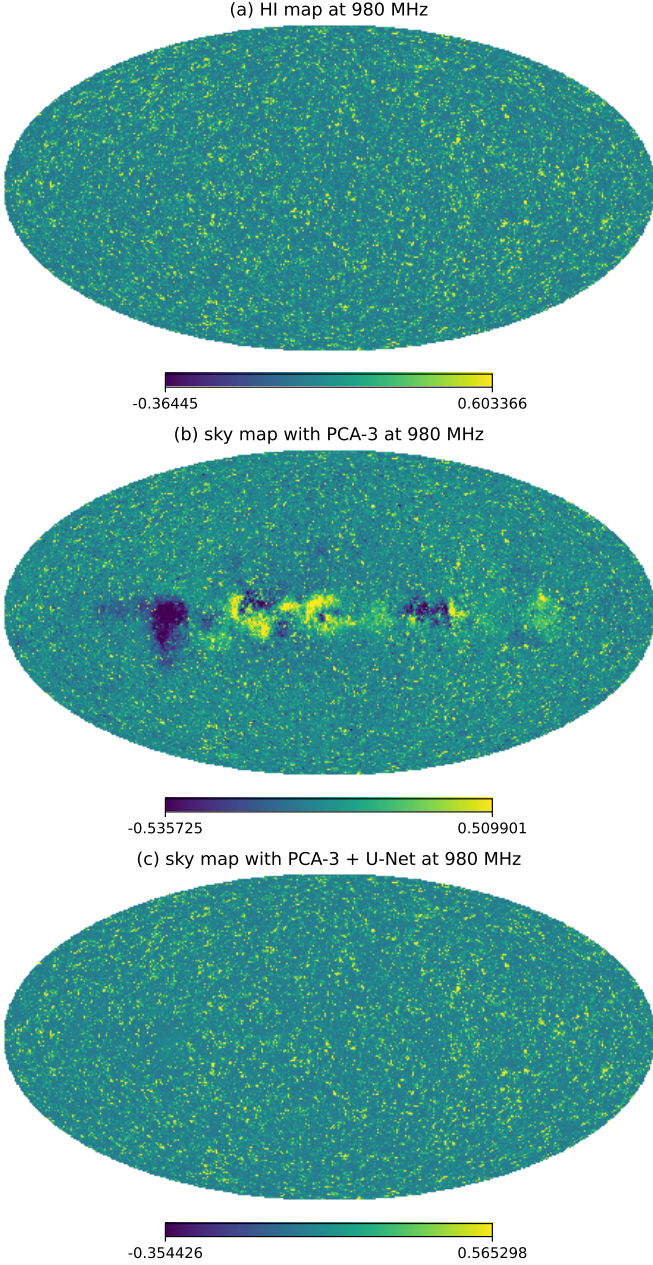


Figure 8. The pixel-wise comparison of the foreground cleaned maps and the input HI map. The polarization leakage parameters are assumed to be $(\epsilon_Q, \epsilon_U) = (0.5\%, 1.0\%)$. Panel (a) shows the input HI map, panel (b) shows the sky map with the first 3 SVD modes subtracted, and panel (c) shows the sky map with additional U-Net processing after subtracting the first 3 SVD modes. As an example, we show only the sky maps at 980 MHz. The unit of each pixel of the sky maps is mK.

The standard data analysis that uses PCA foreground subtraction for HI IM analysis includes signal compensation. Typically, the signal loss is quantified by cleaning a set of simulated pure HI maps using the same foreground subtraction method as that in real data analysis. The compensation is applied to the measurements with a transfer function, which is the power spectrum ratio between the cleaned and uncleaned pure HI map (Switzer et al. 2015; Cunnington et al. 2023; Fornazier et al. 2022). Our simulation analysis shows that such signal compensation can be replaced using U-Net processing. Moreover, the

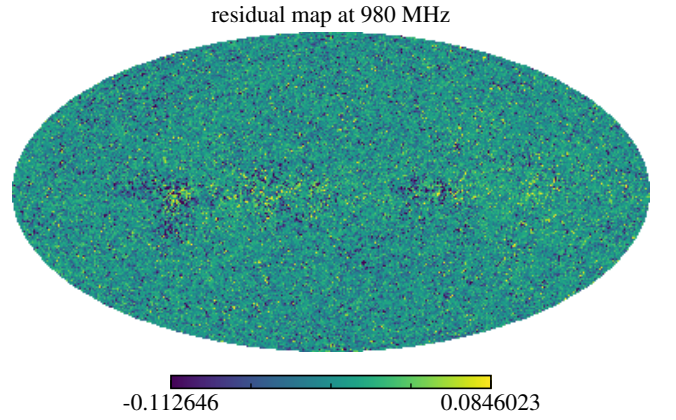


Figure 9. The differential map between the PCA-3 + U-Net cleaned map and the input HI map. The map uses the same polarization leakage parameter assumption as the maps shown in Fig. 8, i.e. $(\epsilon_Q, \epsilon_U) = (0.5\%, 1.0\%)$ and at frequency of 980 MHz. The unit of each pixel of the sky maps is mK.

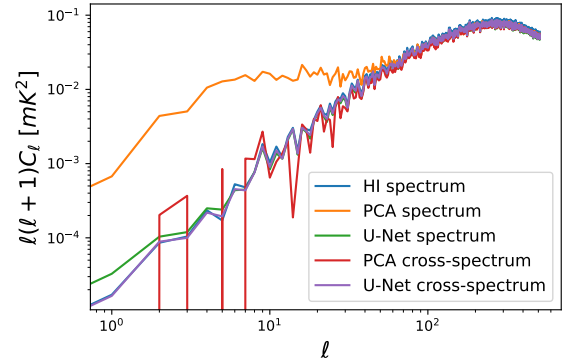


Figure 10. Comparison of the power spectra of foreground cleaned maps with the input HI map. The map uses the same polarization leakage parameter assumption as the maps shown in Fig. 8, i.e. $(\epsilon_Q, \epsilon_U) = (0.5\%, 1.0\%)$. The power spectra are obtained using ten frequency bands averaged to eliminate errors arising from individual frequencies. The blue curve represents the input HI signal. The yellow and green curves represent the results of PCA-3 and PCA-3 + U-Net, and the red and purple curves represent the corresponding cross-correlation power spectra with the input HI map.

signal compensation with U-Net processing works well with different numbers of SVD modes subtraction. It is important to note that the choice of the modes number subtracted in the PCA preprocessing becomes adjustable with the addition of U-Net processing. Specifically, the U-Net processing can reduce foreground residual when using conservative mode subtraction, while compensating for signal loss while using aggressive mode subtraction.

We also highlight that a considerably more complex instrumental effect may be to account for the signal loss in the actual HI IM survey data. The application of actual data analysis requires a comprehensive training set that has as much instrumental effect as possible.

4.4 Robustness analysis

It is known that the training set for supervised deep learning techniques, such as U-Net, must be reasonably close to the real signal. However, the HI fluctuation is under-detected before the foreground

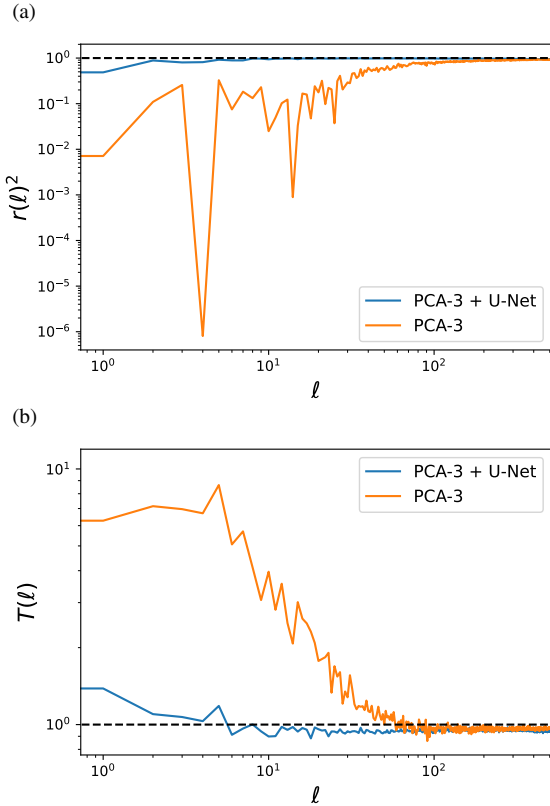


Figure 11. Comparison of the correlation statistic of results with and without U-Net processing, assuming 3 SVD modes subtraction. Panels (a) and (b) show the correlation statistic $r(\ell)^2$ and cleaning error $T(\ell)$, respectively. The results for PCA and PCA + U-Net are shown in yellow and blue curves.

contamination is removed. To determine the robustness of the U-Net foreground subtraction, we aggressively assume that the true HI fluctuation could vary by a few orders in amplitude, i.e. multiplying the initial simulated HI maps by a factor of 0.01, 0.1, 1, 10, and 100 as the test sets, respectively, and apply the same U-Net architecture to such different test sets. We assume the polarization leakage parameter to be $(\epsilon_Q, \epsilon_U) = (0.5\%, 1.0\%)$ and use 4 SVD modes subtracted results as the PCA preprocessing. The cleaning error $T(\ell)$ of the different test sets are shown in Fig. 13 in different colors. It is clear that the cleaning error increases as the HI fluctuation amplitude deviated from the initial HI simulation. The results with the factor of 0.1 and 10 are shown with the yellow and red curves, respectively, which indicates that the cleaning error is negligible with a minor deviation of the modeled HI fluctuation amplitude from the true HI signal. However, if there is a significant deviation in the signal amplitude, i.e. with the factor of 0.01 or 100 as shown with blue or purple curve in Fig. 13, the U-Net foreground subtraction could result in large cleaning error. Therefore, such robustness analysis infers that a successful foreground cleaning with U-Net processing requires the simulated HI fluctuation amplitude to be within the range of 0.1–10 times the true amplitude. The uncertainty of the HI fluctuation amplitude, according to recent measurements, is less than 20% (Cunnington et al. 2023), which is still within the dynamical range where U-Net foreground subtraction processing is reliable.

5 CONCLUSION

The HI IM survey is known as a promising technique for LSS studies. However, the major challenge for HI IM survey is to remove the bright foreground contamination. According to the results of current HI IM survey pilot surveys, as well as the systematic analysis with simulation, it is clear that the secret to successfully removing the bright foreground contamination is to properly control or eliminate the instrumental effect. Due to the instrumental effect’s complexity, it is worthwhile to investigate each one individually. In this work, we propose a deep learning-based foreground subtraction strategy that can eliminate the instrumental effect injected due to systematic polarization leakage.

We generate a set of simulated HI and foreground component maps using the open-source package CRIME. In addition to the intensity maps, we also simulated the Stokes Q and Stokes U maps of the Galactic synchrotron. In our simulation, the polarized HI fluctuation and other foreground contamination are subdominant and disregarded. We also assume the constant polarization leakage fraction across the frequency band and the leakage fraction from Q and U maps are parameterized as ϵ_Q and ϵ_U , respectively. The fraction of polarization leakage needs to be determined according to the observation and can be different between different instruments. In our analysis, we generate a set of simulated sky maps by varying the leakage fraction parameters, i.e. $\epsilon_Q = \{0.0\%, 0.5\%, 1.0\%, 2.0\%\}$ and $\epsilon_U = \{0.0\%, 1.0\%\}$.

We apply the same deep learning architecture, the U-Net, as in our earlier work (Ni et al. 2022) to eliminate polarization leakage. Additionally, the PCA foreground subtraction is compared and used as a preprocessing step for the U-Net foreground subtraction. Our investigation demonstrates that when polarization leakage is present, a conservative PCA foreground subtraction approach produces significant foreground residual, while an aggressive cleaning could remove the foreground residual but result in signal loss. We also tested the differential map and cross-spectrum to ensure that the true HI signal was obtained. On the other hand, the U-Net architecture can successfully remove foreground contamination at different polarization leakage levels.

We also investigate the combination of the U-Net foreground subtraction with different number of mode subtraction in the PCA preprocessing. According to our findings, the additional U-Net processing could either eliminate the foreground residual left over after the conservative PCA foreground subtraction or compensate for the signal loss caused by the aggressive PCA preprocessing. Because of the additional U-Net processing, it becomes flexible to choose the number of modes subtracted in the PCA preprocessing.

Finally, we verify the robustness of the U-Net foreground subtraction strategy by varying the HI fluctuation amplitude of the test set. The results show that within an amplitude range of 0.1–10 times of HI fluctuation amplitude, the U-Net subtraction strategy is reliable.

ACKNOWLEDGEMENTS

We thank Ming Zhang for his helpful discussions and suggestions. We are grateful for the support of the National SKA Program of China (Grants Nos. 2022SKA0110200 and 2022SKA0110203), the National Natural Science Foundation of China (Grant Nos. 11975072 and 11835009), the Liaoning Revitalization Talents Program (Grant No. XLYC1905011), the 111 Project (Grant No. B16009), and the Top-Notch Young Talents Program of China (Grant No. W02070050).

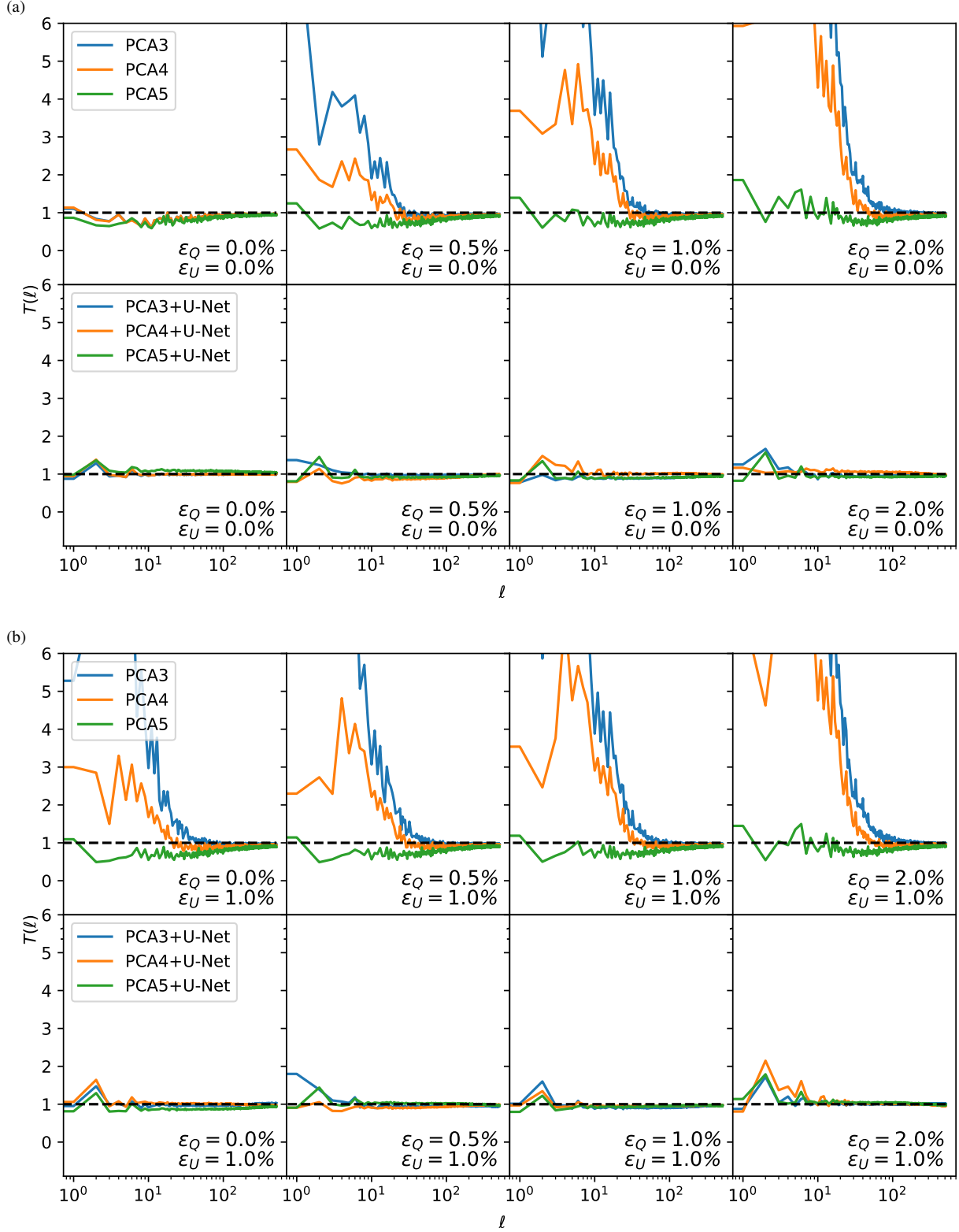


Figure 12. Results of the cleaning errors $T(\ell)$ obtained using U-Net for simulated sky maps of 8 different $[\epsilon_Q, \epsilon_U]$ after PCA-3, PCA-4, PCA-5 processes. The blue, yellow, and green lines represent the input as the result of subtracting 3, 4, and 5 modes from the sky maps using PCA, respectively. The top of each of the two plots is the result of PCA and the bottom is the result of PCA+U-Net.

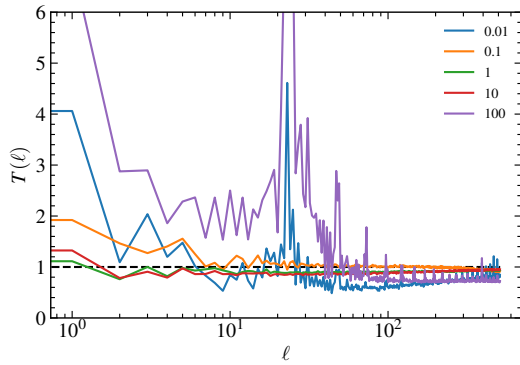


Figure 13. The cleaning error $T(\ell)$ of PCA-4 + U-Net where $(\epsilon_Q, \epsilon_U) = (0.5\%, 1.0\%)$. The blue, yellow, green, red, and purple lines represent the HI signal of the test sets as 0.01, 0.1, 1, 10, and 100 times the original HI signal, respectively.

DATA AVAILABILITY STATEMENT

The data underlying this article will be shared on reasonable request to the corresponding author.

REFERENCES

- Aghanim N., et al., 2020, *Astron. Astrophys.*, 641, A6
- Alam S., et al., 2017, *Mon. Not. Roy. Astron. Soc.*, 470, 2617
- Alonso D., Ferreira P. G., Santos M. G., 2014, *Mon. Not. Roy. Astron. Soc.*, 444, 3183
- Anderson C. J., et al., 2018, *Mon. Not. Roy. Astron. Soc.*, 476, 3382
- Ansari R., et al., 2012, *Astron. Astrophys.*, 540, A129
- Bandura K., et al., 2014, Canadian Hydrogen Intensity Mapping Experiment (CHIME) pathfinder. p. 914522, doi:10.1117/12.2054950
- Battye R. A., Davies R. D., Weller J., 2004, *MNRAS*, 355, 1339
- Battye R. A., Browne I. W. A., Dickinson C., Heron G., Maffei B., Pourtsidou A., 2013a, *Mon. Not. Roy. Astron. Soc.*, 434, 1239
- Battye R. A., Browne I. W. A., Dickinson C., Heron G., Maffei B., Pourtsidou A., 2013b, *MNRAS*, 434, 1239
- Beutler F., et al., 2011, *Mon. Not. Roy. Astron. Soc.*, 416, 3017
- Bhatnagar S., Nityananda R., 2001, *Astron. Astrophys.*, 375, 344
- Bigot-Sazy M. A., et al., 2015, *Mon. Not. Roy. Astron. Soc.*, 454, 3240
- Bobin J., Starck J.-L., Fadili J., Moudden Y., 2007, *IEEE Transactions on Image Processing*, 16, 2662
- Bowman J. D., Morales M. F., Hewitt J. N., 2009, *ApJ*, 695, 183
- Brentjens M. A., de Bruyn A. G., 2005, *Astron. Astrophys.*, 441, 1217
- Britton M. C., 2000, *Astrophys. J.*, 532, 1240
- Bull P., Ferreira P. G., Patel P., Santos M. G., 2015, *Astrophys. J.*, 803, 21
- CHIME Collaboration et al., 2022, arXiv e-prints, p. arXiv:2202.01242
- Chang T.-C., Pen U.-L., Bandura K., Peterson J. B., 2010, *Nature*, 466, 463
- Chapman E., et al., 2012, *Mon. Not. Roy. Astron. Soc.*, 423, 2518
- Chen X., 2012, in International Journal of Modern Physics Conference Series. pp 256–263 (arXiv:1212.6278), doi:10.1142/S2010194512006459
- Cunnington S., Wolz L., Pourtsidou A., Bacon D., 2019, *Mon. Not. Roy. Astron. Soc.*, 488, 5452
- Cunnington S., Irfan M. O., Carucci I. P., Pourtsidou A., Bobin J., 2021, *MNRAS*, 504, 208
- Cunnington S., et al., 2023, *MNRAS*, 518, 6262
- Delabrouille J., et al., 2013, *Astron. Astrophys.*, 553, A96
- Fornazier K. S. F., et al., 2022, *Astron. Astrophys.*, 664, A18
- Gao L.-Y., Zhao Z.-W., Xue S.-S., Zhang X., 2021, *JCAP*, 07, 005
- Gillet N., Mesinger A., Greig B., Liu A., Ucci G., 2019, *Mon. Not. Roy. Astron. Soc.*, 484, 282
- Goodfellow I., Bengio Y., Courville A., 2016, Deep Learning. MIT Press
- Harper S. E., Dickinson C., 2018, *MNRAS*, 479, 2024
- Haslam C. G. T., Salter C. J., Stoffel H., Wilson W. E., 1982, *Astron. Astrophys. Suppl. Ser.*, 47, 1
- He S., Li Y., Feng Y., Ho S., Ravanbakhsh S., Chen W., Póczos B., 2019, *Proc. Nat. Acad. Sci.*, 116, 13825
- Hyvarinen A., 1999, *IEEE Transactions on Neural Networks*, 10, 626
- Jelić V., Zaroubi S., Labropoulos P., Bernardi G., de Bruyn A. G., Koopmans L. V. E., 2010, *MNRAS*, 409, 1647
- Jin S.-J., He D.-Z., Xu Y., Zhang J.-F., Zhang X., 2020, *JCAP*, 03, 051
- Jin S.-J., Wang L.-F., Wu P.-J., Zhang J.-F., Zhang X., 2021, *Phys. Rev. D*, 104, 103507
- Kohl S. A. A., et al., 2018, in NeurIPS.
- Kwon Y., Hong S. E., Park I., 2020, *J. Korean Phys. Soc.*, 77, 49
- Li Y.-C., Ma Y.-Z., 2017, *Phys. Rev. D*, 96, 063525
- Li W., et al., 2019, *Mon. Not. Roy. Astron. Soc.*, 485, 2628
- Li J., et al., 2020, *Science China Physics, Mechanics, and Astronomy*, 63, 129862
- Li Y., Santos M. G., Grainge K., Harper S., Wang J., 2021, *MNRAS*, 501, 4344
- Liao Y.-W., Chang T.-C., Kuo C.-Y., Masui K. W., Oppermann N., Pen U.-L., Peterson J. B., 2016, *Astrophys. J.*, 833, 289
- Lidz A., Furlanetto S. R., Oh S. P., Aguirre J., Chang T.-C., Dore O., Pritchard J. R., 2011, *Astrophys. J.*, 741, 70
- List F., Lewis G. F., 2020, *Mon. Not. Roy. Astron. Soc.*, 493, 5913
- Loeb A., Wyithe S., 2008, *Phys. Rev. Lett.*, 100, 161301
- Loshchilov I., Hutter F., 2017, ArXiv, abs/1711.05101
- Makinen T. L., Lancaster L., Villaescusa-Navarro F., Melchior P., Ho S., Perreault-Levasseur L., Spergel D. N., 2021, *JCAP*, 04, 081
- Mangena T., Hassan S., Santos M. G., 2020, *Mon. Not. Roy. Astron. Soc.*, 494, 600
- Mao Y., Tegmark M., McQuinn M., Zaldarriaga M., Zahn O., 2008, *Phys. Rev. D*, 78, 023529
- Masui K. W., et al., 2013, *Astrophys. J. Lett.*, 763, L20
- Matshawule S. D., Spinelli M., Santos M. G., Ngobese S., 2021, *Mon. Not. Roy. Astron. Soc.*, 506, 5075
- McQuinn M., Zahn O., Zaldarriaga M., Hernquist L., Furlanetto S. R., 2006, *Astrophys. J.*, 653, 815
- Moore D. F., Aguirre J. E., Parsons A. R., Jacobs D. C., Pober J. C., 2013, *ApJ*, 769, 154
- Newburgh L. B., et al., 2016, HIRAX: a probe of dark energy and radio transients. p. 99065X, doi:10.1117/12.2234286
- Ni S., Li Y., Gao L.-Y., Zhang X., 2022, *Astrophys. J.*, 934, 83
- Nunhokee C. D., et al., 2017, *Astrophys. J.*, 848, 47
- Olivari L. C., Remazeilles M., Dickinson C., 2016, *Mon. Not. Roy. Astron. Soc.*, 456, 2749
- Oppermann N., et al., 2015, *Astron. Astrophys.*, 575, A118
- Pacholczyk A. G., 1970, Radio astrophysics. Nonthermal processes in galactic and extragalactic sources
- Patil A. H., et al., 2017, *Astrophys. J.*, 838, 65
- Paul S., Santos M. G., Chen Z., Wolz L., 2023, arXiv e-prints, p. arXiv:2301.11943
- Perdereau O., et al., 2022, *MNRAS*, 517, 4637
- Ronneberger O., Fischer P., Brox T., 2015, CoRR, abs/1505.04597
- Ross A. J., Samushia L., Howlett C., Percival W. J., Burden A., Manera M., 2015, *Mon. Not. Roy. Astron. Soc.*, 449, 835
- Rybicki G. B., Lightman A. P., 1986, Radiative Processes in Astrophysics
- Santos M. G., Cooray A., Knox L., 2005, *Astrophys. J.*, 625, 575
- Santos M., et al., 2015, in Advancing Astrophysics with the Square Kilometre Array (AASKA14). p. 19 (arXiv:1501.03989)
- Santos M. G., et al., 2017, arXiv e-prints, p. arXiv:1709.06099
- Schnitzeler D. H. F. M., Katgert P., de Bruyn A. G., 2009, *Astron. Astrophys.*, 494, 611
- Shaw J. R., Sigurdson K., Pen U.-L., Stebbins A., Sitwell M., 2014, *Astrophys. J.*, 781, 57
- Shaw J. R., Sigurdson K., Sitwell M., Stebbins A., Pen U.-L., 2015, *Phys. Rev. D*, 91, 083514
- Spinelli M., Carucci I. P., Cunnington S., Harper S. E., Irfan M. O., Fonseca J., Pourtsidou A., Wolz L., 2021, *Mon. Not. Roy. Astron. Soc.*, 509, 2048

- Spinelli M., Carucci I. P., Cunningham S., Harper S. E., Irfan M. O., Fonseca J., Pourtsidou A., Wolz L., 2022, *MNRAS*, 509, 2048
- Sun S., et al., 2022, *Research in Astronomy and Astrophysics*, 22, 065020
- Switzer E. R., et al., 2013, *MNRAS*, 434, L46
- Switzer E. R., Chang T.-C., Masui K. W., Pen U.-L., Voytek T. C., 2015, *Astrophys. J.*, 815, 51
- Villanueva-Domingo P., Villaescusa-Navarro F., 2021, *Astrophys. J.*, 907, 44
- Wadekar D., Villaescusa-Navarro F., Ho S., Perreault-Levasseur L., 2021, *Astrophys. J.*, 916, 42
- Wang J., et al., 2021, *MNRAS*, 505, 3698
- Wolleben M., Landecker T. L., Reich W., Wielebinski R., 2006, *Astron. Astrophys.*, 448, 411
- Wolz L., Abdalla F. B., Blake C., Shaw J. R., Chapman E., Rawlings S., 2014, *Mon. Not. Roy. Astron. Soc.*, 441, 3271
- Wolz L., et al., 2015, *PoS*, AASKA14, 035
- Wolz L., et al., 2017, *MNRAS*, 464, 4938
- Wolz L., et al., 2021, arXiv e-prints, p. [arXiv:2102.04946](https://arxiv.org/abs/2102.04946)
- Wu P.-J., Zhang X., 2022, *JCAP*, 01, 060
- Wu F., et al., 2021, *MNRAS*, 506, 3455
- Wu P.-J., Shao Y., Jin S.-J., Zhang X., 2022a, ArXiv, [abs/2202.09726](https://arxiv.org/abs/2202.09726)
- Wu P.-J., Li Y., Zhang J.-F., Zhang X., 2022b, ArXiv, [abs/2212.07681](https://arxiv.org/abs/2212.07681)
- Xu Y., Zhang X., 2020, *Sci. China Phys. Mech. Astron.*, 63, 270431
- Xu Y., Wang X., Chen X., 2015, *Astrophys. J.*, 798, 40
- Yohana E., Li Y.-C., Ma Y.-Z., 2019, *Res. Astron. Astrophys.*, 19, 186
- Zhang J.-F., Gao L.-Y., He D.-Z., Zhang X., 2019, *Phys. Lett. B*, 799, 135064
- Zhang J.-F., Wang B., Zhang X., 2020, *Sci. China Phys. Mech. Astron.*, 63, 280411
- Zhang M., Wang B., Wu P.-J., Qi J.-Z., Xu Y., Zhang J.-F., Zhang X., 2021, *Astrophys. J.*, 918, 56
- de Bruyn A. G., Katgert P., Haverkorn M., Schnitzeler D. H. F. M., 2006, *Astronomische Nachrichten*, 327, 487
- de Villiers M. S., Cotton W. D., 2022, *Astron. J.*, 163, 135
- van Straten W., 2004, *ApJS*, 152, 129

This paper has been typeset from a $\text{\TeX}/\text{\LaTeX}$ file prepared by the author.